ORIGIN OF MAGNETIC LINEATIONS ON MARS

NASA MARS DATA ANALYSIS PROGRAM

NAG5-9799

FINAL REPORT

September 23, 2002

Robert E. Grimm, Principal Investigator
Laboratory for Atmospheric and Space Physics
University of Colorado
Boulder, CO

bob.grimm@lasp.colorado.edu
CU Project #1532973

1. SUMMARY

The magnetic lineations discovered by MGS have been considered to be evidence of early plate tectonics on Mars. However, the lineations approximately follow lines of latitude, i.e., small circles. This presents significant geometrical problems for plate-like spreading, particularly at high latitudes. However, the sublatitudinal orientation of the lineations is consistent with meridianal extension and perhaps limited crustal spreading due to a stress event centered near the geographic pole. We hypothesize that this event was the early formation of the crustal dichotomy through mantle-convective processes. This could have taken the form of a southern megaplume that formed the thick highlands crust or as subduction or downwelling in the north. Both would result in tensional stresses in the south that would form extensional fractures perpendicular to the CM-CF offset. The observed magnitude and distribution of magnetization indicates that crustal intrusion associated with this major mantle-convective event resulted in ~1000 km of extension in the southern highlands. Subsequent spin-axis reorientation due to loss of crust in the north or gain of crust in the south brough the CM-CF offset into its present N-S alignment. A portion of the ancient valley networks observed in the southern highlands are spatially associated with crustal magnetism and are quantitatively shown to be consistent with hydrothermal discharge over crustal intrusions.

2. TABLE OF CONTENTS

3. INTRODUCTION

The remarkable magnetic anomalies discovered by the Mars Global Surveyor (*Acuña et al.*, 1999; Figure 1) strongly suggest that early Mars had an intrinsic magnetic field and that newly created crust was magnetized by thermoremanence. The large magnitude and size of the anomalies further indicates that the tectonic processes that influenced their formation were global in scale. *Connerney et al.* (1999) have suggested that this process was plate tectonics, a hypothesis that has received widespread attention. They based this hypothesis qualitatively on the apparent linear nature of the magnetic anomalies, which was considered to be similar to terrestrial magnetic "stripes" formed by seafloor spreading. Connerney and co-workers further showed through simple modeling that the intensity of magnetization had to be relatively strong compared to terrestrial analogs in order to reproduce the large magnetic fields observed from orbit.

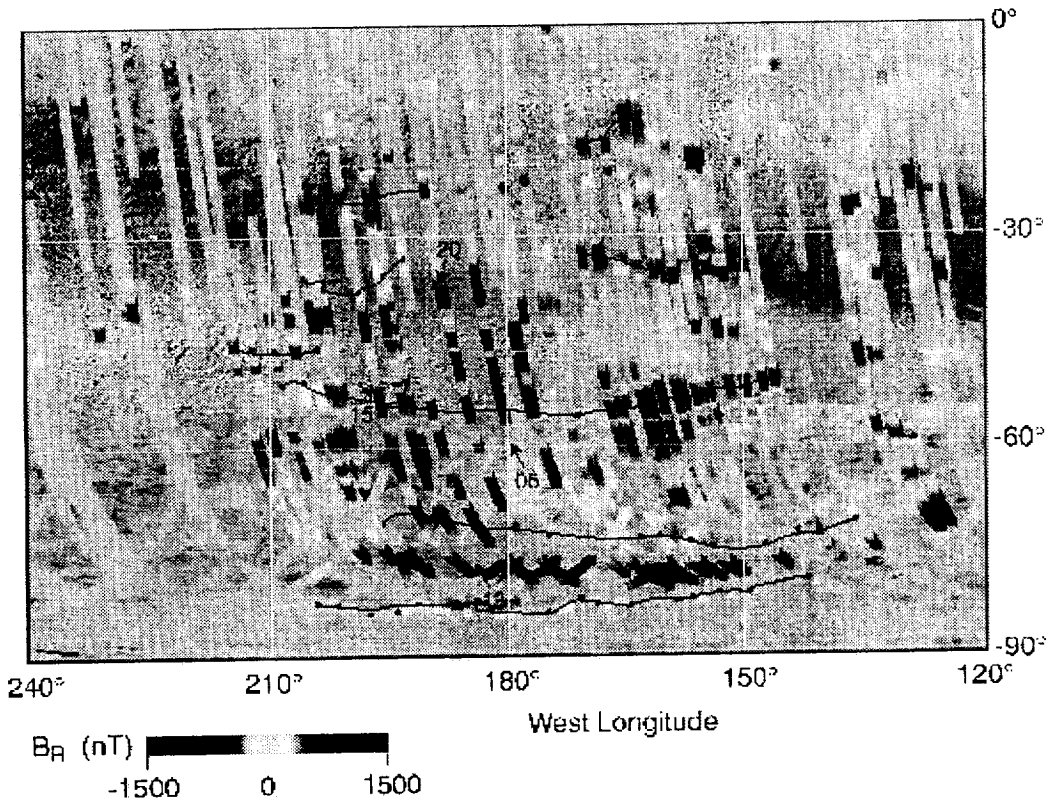

Figure 1. Magnetic field measured by MGS, from *Connerney et al.* (1999). Note strong sublatitudinal orientation to the lineations. Solid lines and dots denote segments used for geometric analysis (see below).

Plate tectonics has been such a successful theory on Earth because, like all good theories, it has strong predictive power. These predictions follow from the simplicity of rigid-plate motion on a sphere, which constrains the geometry of plate interactions. In general, spreading centers are not constrained to follow any particular orientation, although a great-circle path is required for normal spreading (when movement is perpendicular to the segment orientation). A second basic observation that can be made in addition to their linearity is that the anomalies approximately follow lines of latitude (Figure 1.), i.e, small circles. Especially at high latitudes, this presents strong geometrical problems for plate spreading, and suggests that other, alternative hypotheses should be considered.

Any such alternative process must be able to produce dominantly meridianal extensional stresses over at least the latitudinal band in which the magnetic anomalies are observed, large strain (presumably tens to hundreds of percent or more; see below), and be limited to the Noachian era (as the lineations are observed only in the heavily cratered southern hemisphere). Potential candidates are global expansion, true polar wander, despinning, and formation of the "hemispheric dichotomy." While expansion produces extensional stress, such stress is not limited to a meridianal direction; furthermore the strain for plausible expansion is very small (see Solomon, 1979). Polar wander can be rejected for similar reasons (see *Melosh,* 1980; *Grimm and Solomon*, 1986). Despinning does produce a zone of east-west normal faulting at latitudes higher than 36° (*Pechmann and Melosh*, 1979), but the martian anomalies exceed this range, and plausible changes in flattening still produce total hemispheric extension limited to tens of kilometers.

Mars is divided by a "hemispheric dichotomy" into heavily cratered southern highlands and resurfaced northern lowlands. Leading hypotheses for this dichotomy encompass both internal (mantle convection: *Lingenfelter and Schubert*, 1973; *Wise et al.*, 1979) and external (impact: *Wilhelms and Squyres*, 1984) mechanisms. However, MGS measurements of martian topography (*Smith et al.*, 1999) reveal that much of the difference in elevation between the south and north is due to the center-of-mass/center-of-figure (CM-CF) offset. This degree-one offset corresponds to a steady downward slope of 0.036° between the south and north poles, and strongly favors a "smooth" internal process for the formation of the hemispheric dichotomy. We suggest that the north-south CM-CF offset is not coincidence, but the result of spin-axis reorientation due to mantle-convective formation of the hemispheric dichotomy, and that the orientation of magnetic anomalies along lines of latitude is a result of meridianal extension of hundreds of kilometers or more associated with this major geological event in the early history of Mars.

The objectives of this project were to (1) Quantify the planform and intensity of crustal magnetization, (2) Assess how these geometrical patterns constrain models for the formation of the magnetization, particularly the origin of the crustal dichotomy, (3) Explore the relationships, if any, of crustal magnetization to surface geology, in particular, the valley networks.

4. MAGNETIC MODELING

Inversion of the pattern of crustal magnetization from magnetic anomalies is the foundation for determining the time scale for geomagnetic reversals and measurement of seafloor spreading (*Vine and Matthews*, 1963). The crustal magnetism is preferred to the magnetic anomalies themselves because superposition of the anomalies of adjacent blocks with differing magnetization intensities and/or directions results in a complex signal that may not be visually interpretable; furthermore induced moments distort the observed field and the inferred positions of reversals. Although the effects of induced magnetism may be ruled out for Mars (its crustal magnetism must be wholly remanant in the absence of a present-day intrinsic field), reduction of the observed data to the actual magnetization is an important step in understanding the origin of the magnetic anomalies.

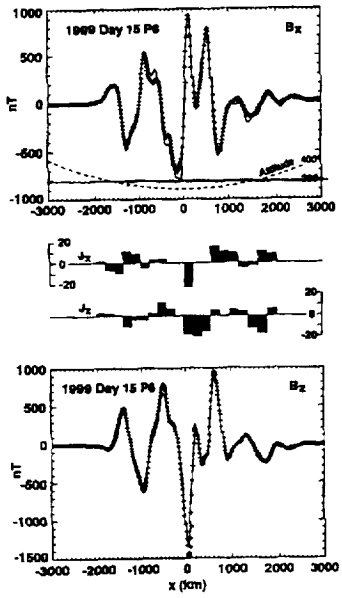

Connerney et al. (1999) presented simple models for several individual MGS orbits. Their model is based on the following assumptions: (1) magnetization is two-dimensional, (2) magnetization is constant in crustal blocks 200 km wide by 30 km thick, and (3) the two components of magnetization J_x and J_z are allowed to vary independently. These models reproduce the observed anomalies quite accurately (Figure 2). As acknowledged by these authors, however, this is only one possibility for the actual crustal magnetization

Figure 2. Horizontal (top) and vertical (bottom) magnetic anomalies with inferred horizontal and vertical crustal magnetization (middle), from *Connerney et al.* (1999).

We independently modeled two of the orbits presented by *Connerney et al.*(1999). The data were digitized from the published paper. We also used a generalized inverse using singular-value decomposition to solve for the crustal magnetization. Our results for orbit 1999 Day 15 P6, also using an unconstrained J_x, J_z model, are very similar to those of Connerney and co-workers (Figure 3). This result was obtained for a relatively low damping factor (SV cutoff ratio) of 10^{-2}. A similar comparison was obtained for orbit 1999 Day 20 P7.

We performed a more thorough exploration of the parameter space for this model than reported by *Connerney et al.* (1999). We are examined the effects of varying block thickness, block width, and the damping factor on the goodness-of-fit, the model roughness, and the maximum magnetization. We found, as expected, that goodness-of-fit and model roughness are inversely related through the damping parameter. Because Connerney and co-workers emphasized the best fits to the data, their models are relatively rough. *Connerney et al.* (1991) state that "reversals in the direction of magnetization of adjacent blocks are common, if not the rule." However, strong variations between adjacent model blocks is almost always a signature of excessively high model variance or roughness. Reversals would be more believable if groups of at least several model blocks had the same sign, which can be achieved by using a narrower

block and a higher damping. We find that goodness-of-fit is insensitive to block thickness but does improve with narrower blocks (because there are more free parameters) but that, conversely, model roughness does not vary as strongly with block width as it does with block thickness. The maximum crustal magnetizations, already apparently extreme for the nominal model of Connerney and co-workers, increase as the blocks are thinned.

While the models of *Connerney et al.* (1991) were useful as exploratory tools to describe the general magnitude of crustal magnetization, the spatial patterns of this magnetization are random and unrealistic (Figure 3). This is because J_x and J_z are both allowed to vary independently. In reality, the magnetic inclination will vary with absolute plate motion and true polar wander, but is often considered constant for some number of geomagnetic reversal cycles of seafloor spreading. Alternatively, if there is no plate motion and polar wander, the magnetizing field should closely approximate a global dipole. We have tested this latter hypothesis by constraining $J_x/J_z = 0.5 \tan(\Theta)$, where Θ is the geomagnetic colatitude. The magnetization amplitude (positive or negative) for each block remains as a free parameter. The solved magnetizations now vary smoothly (Figure 5) and, because the model is more tightly constrained, the required intensity of magnetization is less than half that of the free J_x,J_z model. The cost is a modest decrease in goodness-of-fit (Figure 6) which, while statistically significant, does not detract from the plausibility of the model.

Table 1. Summary of Magnetic-Modeling Fits to MGS Magnetometer Data.

	Fit (%)	J_{max} (A/m)	Pole
1999/15/P6			
Arbitrary	**98**	**41**	**-**
Dipole +/-	**95**	**20**	**18 N**
Dipole + only	**91**	**55**	**8 S**
Const. Incl.	**95**	**27**	**19 N**
1999/20/P7			
Arbitrary	**96**	**34**	**-**
Dipole +/-	**93**	**41**	**57 S**
Dipole + only	**90**	**61**	**47 S**
Const. Incl.	**93**	**35**	**54 S**

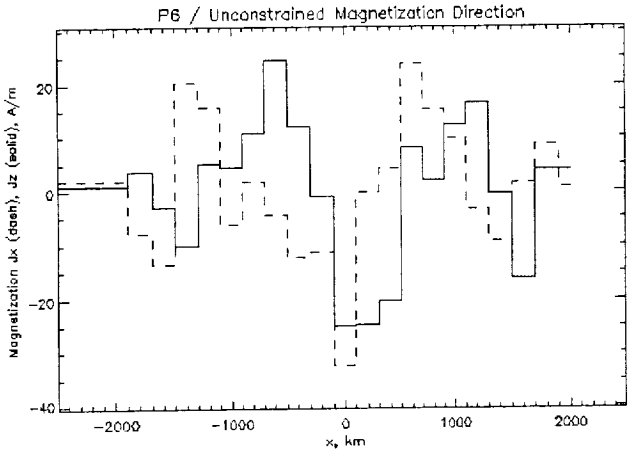

Figure. 3. Best-fitting crustal magnetization for orbit 1999 Day 15 P6. The model formulation closely follows that of Connerney et al. (1999). The magnetization directions of each block are unconstrained, i.e., the x- and z- magnetizations vary independently. Note close match to the result of *Connerney et al.* (1999) (Fig. 2 above). However, when magnetizations are plotted as vectors, a random, unrealistic magnetizing field is inferred.

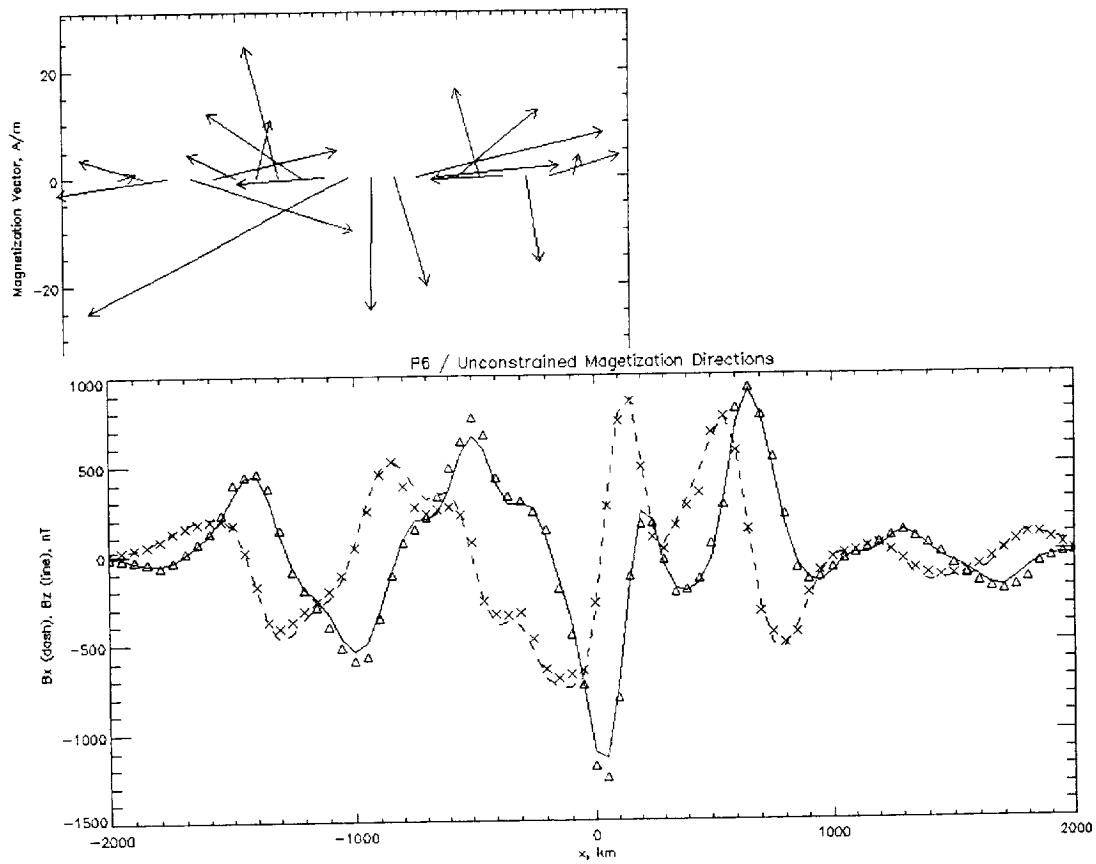

Figure 4. Data (symbols) and 2D model fit (lines) to magnetic field for model in previous figure. Goodness-of-fit is 98.4%.

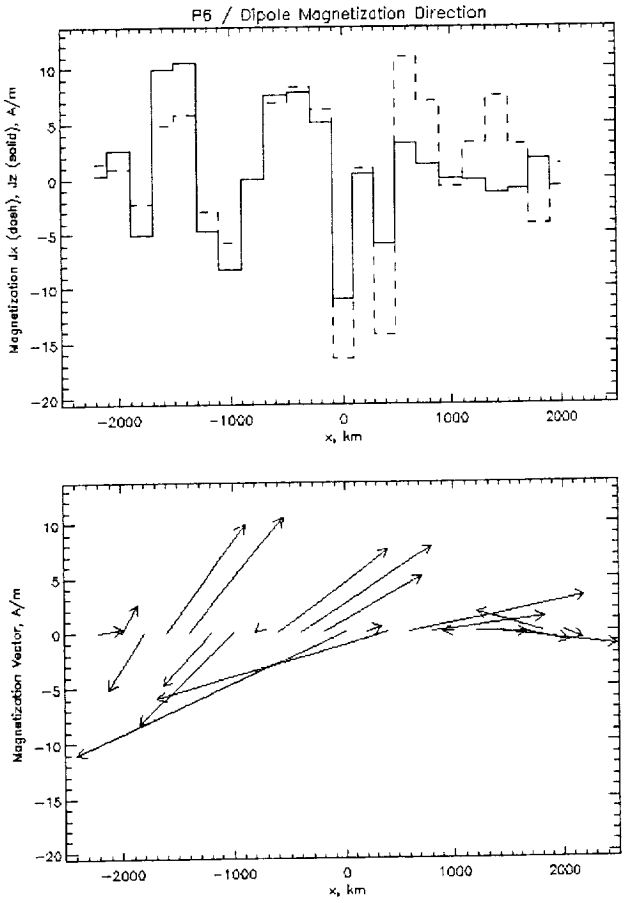

Figure. 5. Best-fitting crustal magnetization for same data as above, except magnetization directions are constrained to follow a global dipole. The latitude of the magnetic pole is a new free parameter, but each of the model blocks now has only one free parameter (the total magnetization) instead of two. The maximum magnetization in the constrained model is about half that of the unconstrained model (20 vs 42 A/m). The apparent magetic equator is near x=+1000 km (where the magnetizations are nearly horizontal) and corresponds to a magnetic pole near 54 °N, 16 °W.

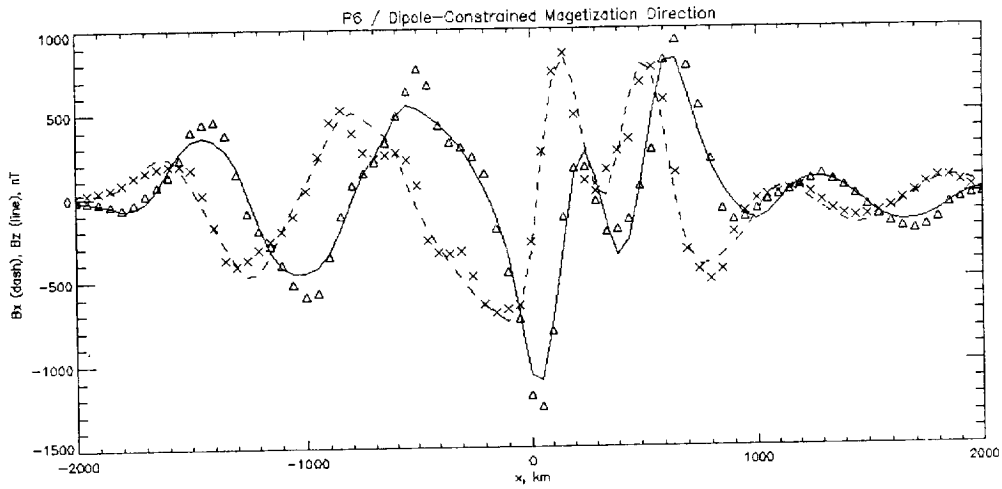

Figure 6. Data (symbols) and 2D model fit (lines) to magnetic field for model in which magnetization direction is constrained to follow a global dipole. Goodness-of-fit is 94.5%.

While the 2D models have lead to useful understanding of the crustal magnetization of Mars (see below), continuity between orbit tracks cannot be enforced, whereas the linear nature of the magnetic anomalies suggests that such continuity exists. In order to understand fully the spatial relationships of magnetization, 3D models are necessary. This was an important goal of our original proposal that was not attained. The primary responsibility lies with the PI, largely because constant supervision was not possible owing to the distance separating the PI's workplace and the graduate student at the performing institution. Secondary issues were the lack of an available student during the first year of this project and the subsequent ability and experience of that student in performing geophysical inversions. To reduce commitments to a level that could be managed at the PI's ability to interact with the performing institution, the program there was descoped to a single graduate student. This senior student carried out the work described in the attached reprint to this report. During the period of this contract, other groups have produced planform-magnetization models (*Prurucker et al.*, 2000; *Arkani-Hamed*, 2002, *Cain et al.*, 2002)

5. STRAIN ASSOCIATED WITH MAGNETIC ANOMALIES

The magnetizatio models can be used as the basis for estimating the amount of extension under meridianal stress. We assume that such extension and intrusion occurred while the martian geodynamo was active, but that the intrinsic was field was zero at other times. We next assume that the maximum observed magnetization intensity corresponds to a model block that is entirely composed of intruded, magnetized, igneous rocks. This is an upper limit, as even the most magnetized block could still contain unmagnetized material. It is also implicitly assumed that the scale of mixing of magnetized and unmagnetized rock is small compared to the block width. Under these assumptions, the extension of each block is proportional to the block magnetization, and the total extension over the profile can be computed. For the result shown in Figure 5, the extension is 1550 km, or a strain of 59% to produce the present-day profile length of 4000 km. While this amount of strain is large compared to that expected from vertical tectonics alone, it is only moderately larger than that inferred for deep-seated extension of the Valles Marineris (10-30%; *Anderson and Grimm*, 1998) and yet is small compared to the essentially unbounded extension that occurs for plate tectonics. The minimum extension estimated from the models above is 830 km, or 26% strain.

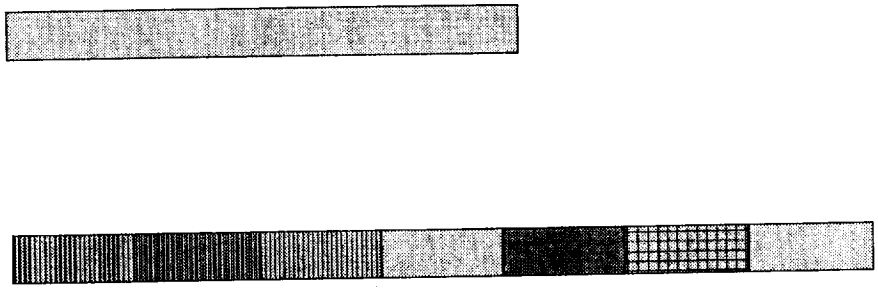

Figure 8. Schematic illustration of assumed relationship between magnetization intensity and crustal strain.

6. GEOMETRICAL TESTS

The paleomagnetic record of Mars can be used in several ways to test the predictions of the plate-tectonic and hemispheric-dichotomy hypotheses. The predictive power of the theory of plate tectonics lies in the simplicity of its geometric rules for rigid motions on the surface of a sphere (*McKenzie and Parker*, 1967; *Morgan*, 1968), and this theory can be applied to Mars. All plate movements occur along small circles about some apparent rotation pole, and where a plate boundary lies in the direction of motion a transform fault results. Therefore the orientation of transform faults is the most robust method of determining the geometry of relative rotation between two plates. *Grimm and Solomon* (1989) applied this method to putative fracture zones on Venus. If the crustal magnetization reconstructions described above are sufficiently robust and strike discontinuities are observed, then we will test to see if they satisfy the geometrical requirements of transform faults.

Ridges and trenches are not geometrically constrained. Where convergent or divergent motions are perpendicular to a plate boundary, however, that boundary will lie along a great circle. Regardless of spreading direction, the spreading rate must be proportional to sin(Δ), where Δ is the angular distance to the rotation pole. This is the second-best method of determining plate geometry. The third method, earthquake focal mechanisms, is less reliable and is neither available for Mars nor appropriate to paleomotion studies.

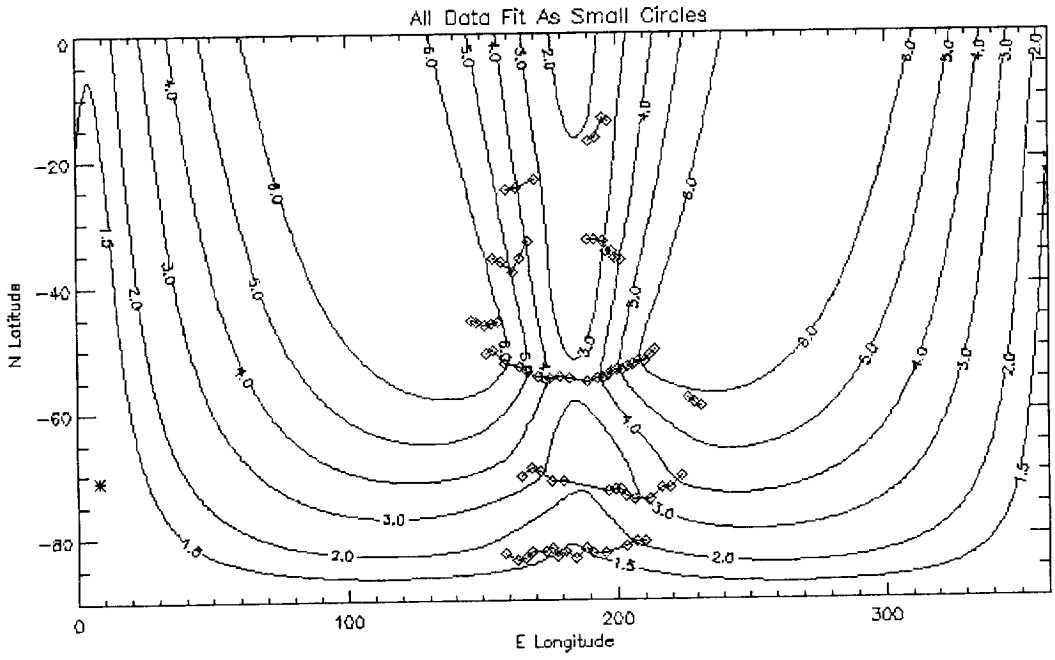

Figure 7. Map of RMS deviations (degrees) for trial southern poles about which magnetic lineations (connected diamonds) are tested as small circles. Best fit is 71 S, 8 E (asterisk); proximity to the geographic pole simply confirms the sublatitudinal orientation of the lineations.

Working directly with the modeled planform of magnetization, we can examine along-strike variations in the widths of anomalies which could be a manifestation of a sin(Δ) spreading-rate variation. We can also test whether segments lie along great circles, which would indicate normal spreading. Clearly smaller segments can be arbitrarily well fit to a great circle, whereas transform faults and/or oblique spreading could render the test invalid for larger segments. As the former dominate apparent ridge directions on Earth, arcs that do not fit great circles should show transform offsets if plate tectonics is still satisfied (e.g., Southeast-Indian and Pacific-Antarctic Ridges on Earth are grossly east-west, but are strongly segmented).

While there are a number of tests for plate tectonics, the global dichotomy model as presently formulated requires only that the crustal magnetizations all follow small circles. For such a test (Figure 1), we find an apparent pole at 71 S, 352 W (71 N, 172 W), with an RMS arc deviation of 1.2 degrees (Figure 7). The longitude is not particularly meaningful, as it is determined by the distribution of the data, but the latitude and goodness-of-fit confirms the visual impression that the lineations follow small circles, apparently around some former source beneath the Vastitas Borealis.

The bilateral symmetry of magnetization that was the hallmark of seafloor spreading is not immediately obvious in the martian lineations, although the subtle arc shapes to the positive anomaly bands 35 S (concave to the south) and 55 S (concave to the north) suggests symmetrical spreading about a rotation pole located close by. We have tested the bilateral symmetry of magnetization using established statistical techniques (*Grimm and Solomon*, 1989). Typical correlations ~0.65 (Figure 8) do not strongly support the concept of bilateral, plate-like intrusion and spreading. Rather, the magnetic anomalies were probably formed by serial, perhaps spatially random magmatic intrusions.

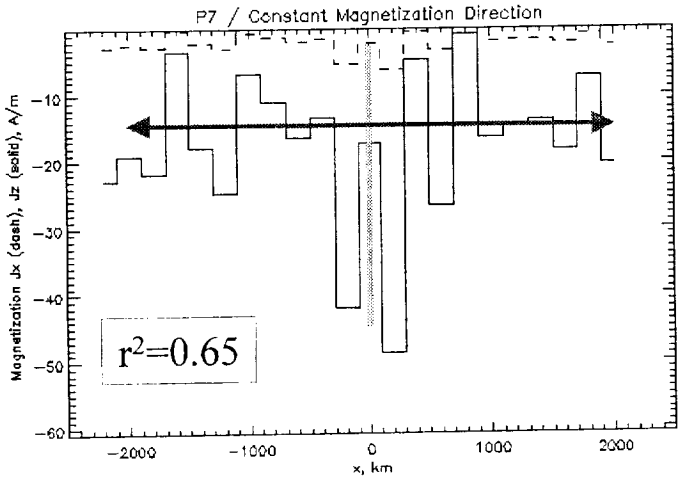

Figure 8. Bilateral symmetry test for plate tectonics. Each modeled magnetic block is assumed to be a spreading center and the correlation coefficient calculated around it to the maximum possible distance.

7. SYNTHESIS: GLOBAL MODELS FOR THE ORIGIN OF MAGNETIC LINEATIONS

We review all alternative hypotheses for the origin of magnetic lineations on Mars and, by process of elimination, assess those that remain most likely.

Plate Tectonics. This is the original hypothesis of *Connerney et al.* (1999). Arbitrarily large (unconstrained) crustal extension and intrusion is allowed. An unmapped location for subduction is required to conserve area. There are strong geometrical constraints to motion for rigid lithosphere, including the fit of lineation arcs to great circles and bilateral symmetry of lineations. Neither of these constraints is satisfied for the martian magnetization. Finally, a near-constant crustal thickness should be produced by decompression melting, but gravity data indicates a strong gradient in crustal thickness in the southern highlands (*Zuber et al.*, 2000). We conclude that earth-like plate-tectonics did not form the magnetic lineations.

Tharsis Tectonics. The load from Tharsis is known to have deformed the crust to great distances; could it also have led to the magnitude and direction of the magnetic lineations? Two prominent lineations can indeed be fit to great circles with centers near Tharsis, but the anomaly pattern as a whole does not follow Tharsis radials. Furthermore, strains from such loading, or "vertical tectonics," are expected to be much smaller, in the range of a few percent; recall that the strain associated with the lineations is of order ten percent or more.

Spin Tectonics. This includes faulting due to the shift of the rotational bulge during spin-axis reorientation or polar wander and the relaxation of the rotational bulge due to tidal despinning. For the former, we expect N-S oriented extensional structures near the paleopole and only moderate strains (several %, e.g., *Grimm and Solomon*, 1986). For the latter, E-W oriented fractures can occur, but they are restricted to poleward of 36° from the equator (*Pechmann and Melosh*, 1979). The magnetic lineations of Mars fail the geometrical tests for both of these models.

Northern Crustal Depletion. Subduction or other crustal recycling is one hypothesis for formation of the global dichotomy. In this scenario, "back-arc" tensional stresses might be set up in the south, which would cause strong gradients in extension, intrusion, magnetization. The expected strain magnitude unknown, but it would likely be bigger than vertical or spin tectonics but less than plate tectonics: this is consistent with moderately large strains inferred for the magnetic lineations.

Southern Crustal Accretion. This is an alternative hypothesis for formation of the global dichotomy in which the a megaplume results in generation of a massive crustal plateau. This is consistent with the basaltic composition of the southern crust (*Christiansen et al.*, 1999) and indeed is facilitated by a 2.6x gravity-scaled efficiency for decompression melting (*McKenzie*, 1999). Melt thicknesses of several tens of km result from several tens of km extension (see *Grimm and Hess*, 1997) at hotter Noachian mantle temperatures (*Schubert et al.*, 1992). A southern megaplume could generate large, latitudinally varying crustal thickness (80 km at S. pole to 35 km at N. plains boundary; *Zuber et al.*, 2000). Radial extension over the uplift causes

circumferential extension fractures (*Banerdt et al*, 1982); subsequent melt intrusion and solidification would form the magnetic lineations. This model is most consistent with all available data.

In either the northern-depletion or southern-accretion models, the center of mass (CM) becomes displaced from the center of figure (CF), resulting in a spin inbalance. Polar wander then brings the CM-CF offset into alignment with the spin axis, i.e., to a N-S configuration. The near-perfect N-S alignment of the CM-CF offset has not heretofore been explained.

Figure 9 (on following page) illustrates the northern-depletion and southern-accretion models with subsequent spin-axis realignment.

8. RELATION OF CRUSTAL MAGNETISM TO SURFACE GEOLOGY

The spatial distribution of crustal magnetization is statistically correlated to the locations of Noachian, southern-highlands valley networks. We hypothesize that at least some of these valley networks were carved by hydrothermal discharge over the cooling intrusions represented by the magnetization. To test this hypothesis, a numerical model for hydrothermal discharge on Mars was formulated and calibrated; a by-product is a better understanding of the physical controls on hydrothermal discharge as well as quantitative constraints on crustal permeability imposed by geochemistry. We found that the total discharge due to intrusions building that part of the southern highlands crust associated with valley networks is comparable to the discharge inferred from valley geometry, supporting the hypothesis. Details are given in the attached reprint.

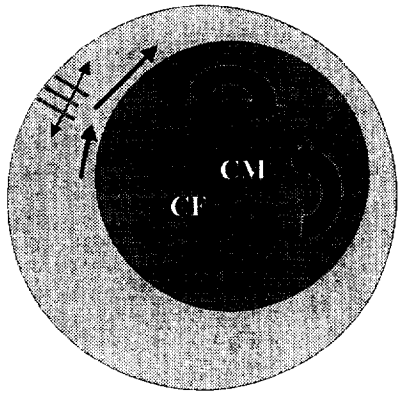

Northern Crustal Depletion (Downwelling) model for formation of magnetic lineations through "back-arc" extension. Crust: green, mantle: red, lineations (in cross-section), red line; CM, center of mass; CF, center of figure.

Southern Crustal Accretion (upwelling) model for magnetic lineations through extension above megaplume.

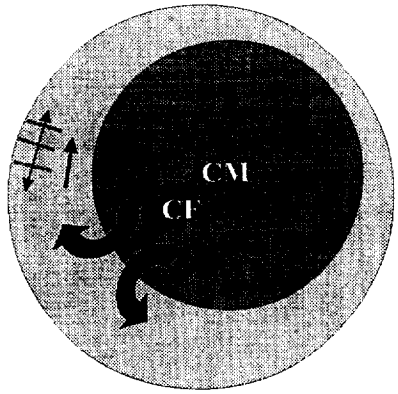

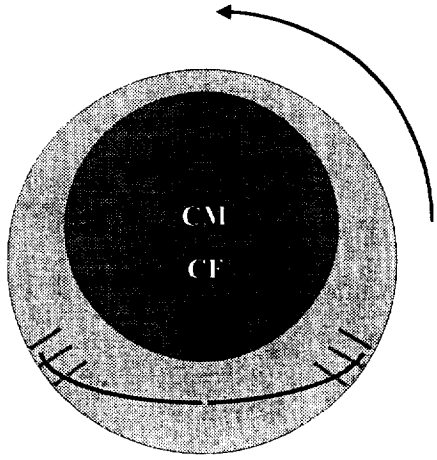

Spin-axis reorientation due to loss of crust in north or gain of crust in south brings CM-CF offset into N-S alignment, also brings magnetic lineations into sublatitudinal orientation.

5. REFERENCES

Acuña, M.H., and 12 others, Global distribution of crustal magnetization discovered by the Mars Global Surveyor MAG/ER experiment, *Science, 284*, 790-793, 1999.

Anderson, S., and R.E. Grimm, 1998, Rift processes at the Valles Marineris, Mars: Constraints from gravity on necking and rate-dependent strength evolution, *J. Geophys. Res., 103,* 11,113-11,124.

Arkani-Hamed, J., Magnetization of the Martian crust, *J. Geophys. Res., 107*, NO. E5, 10.1029/2001JE001496, 2002.

Banerdt et al. (1982) *JGR, 87*, 9723.

Cain, J. et al. (in press), Journal of Geophysical Research-Planets.

Christiansen et al. (1999) *AGU Fall Mtg.*, P12B-05.

Connerney, J.E.P., and 9 others, Magnetic lineations in the ancient crust of Mars, *Science, 284,* 794-798, 1999.

Grimm and Hess (1997) in *Venus II* (eds. Bougher et al.), p. 1205.

Grimm, R.E., and R.J. Phillips, Anatomy of a venusian hot spot: Geology, gravity, and mantle dynamics of Eistla Regio, *J. Geophys. Res., 97,* 16035-16054, 1992.

Grimm, R.E., and S.C. Solomon, Tectonic tests of proposed polar wander paths for Mars and the Moon, *Icarus, 65*, 110-121, 1986.

Grimm, R.E., and S.C. Solomon, Tests of crustal divergence models for Aphrodite Terra, Venus, *J. Geophys. Res., 94,* 12103-12131, 1989.

Herrick, R. R., and R. J. Phillips, Geological correlations with the interior density structure of Venus, *J. Geophys. Res., 97,* 16,017-16,034, 1992.

Lingenfelter, R. E., Schubert, G., Evidence for convection in planetary interiors from first-order topography, Moon, 7, 172-180, 1973.

McKenzie (1999) *Nature, 399*, 307.

McKenzie, D.P., and R.L. Parker, The North Pacific: An example of tectonics on a sphere, *Nature, 216*, 1276-1280, 1967.

Melosh, H.J., Tectonic patterns on a reoriented planet, *Icarus, 44,* 745-751, 1980.

Morgan, W.J., Rises, trenches, great faults, and crustal blocks, *J. Geophys. Res., 73,* 1959-1982, 1968.

Pechmann, J.B., and H.J. Melosh, Global fracture patterns of a despun planet, *Icarus, 38,* 243, 1979.

Purucker M. et al. (2000) *Geophysical Research Letters, 27*, 2449-2452.

Richards, M. A., and B. H. Hager, Geoid anomalies in a dynamic Earth, *J. Geophys. Res., 89,* 5987-6002, 1984.

Schubert et al (1992) in *Mars* (eds Kieffer et al), p. 147.

Smith, D.E., and 18 others, The global topography of Mars and implications for surface evolution, *Science, 284,* 1495-1503, 1999.

Solomatov, V. S., and L.-N. Moresi, Stagnant lid convection on Venus, *J.Geophys. Res., 101,* 4737-4753, 1996.

Solomon and Head (1982) *JGR, 87,* 9755.

Solomon, S.C., The relationship between crustal tectonics and interior evolution in the Moon and Mercury, *Phys. Earth Planet. Inter., 15,* 135-145, 1979.

Vine, F.J., and D.H. Matthews, Magnetic anomalies over oceanic ridges, *Nature, 199,* 947-949, 1963.

Wilhelms, D.E., and S. Squyres, The Martian hemispheric dichotomy may be due to a giant impact, *Nature, 309,* 138-140, 1984.

Wise, D.U., M.P. Golombek, and G.E. McGill, Tectonic evolution of Mars, *J. Geophys. Res., 85,* 7934-7939, 1979.

Zuber et al. (2000) *Science, 287*, 1788

JOURNAL OF GEOPHYSICAL RESEARCH, VOL. 107, NO. E5, 10.1029/2001JE001616, 2002

Controls on Martian hydrothermal systems: Application to valley network and magnetic anomaly formation

Keith P. Harrison
Laboratory for Atmospheric and Space Physics, University of Colorado, Boulder, Colorado, USA

Robert E. Grimm
Laboratory for Atmospheric and Space Physics, University of Colorado, Boulder, Colorado, USA
Blackhawk Geoservices, Inc., Golden, Colorado, USA

Received 11 September 2001; revised 18 December 2001; accepted 3 January 2002; published 3 May 2002.

[1] Models of hydrothermal groundwater circulation can quantify limits to the role of hydrothermal activity in Martian crustal processes. We present here the results of numerical simulations of convection in a porous medium due to the presence of a hot intruded magma chamber. The parameter space includes magma chamber depth, volume, aspect ratio, and host rock permeability and porosity. A primary goal of the models is the computation of surface discharge. Discharge increases approximately linearly with chamber volume, decreases weakly with depth (at low geothermal gradients), and is maximized for equant-shaped chambers. Discharge increases linearly with permeability until limited by the energy available from the intrusion. Changes in the average porosity are balanced by changes in flow velocity and therefore have little effect. Water/rock ratios of ~0.1, obtained by other workers from models based on the mineralogy of the Shergotty meteorite, imply minimum permeabilities of 10^{-16} m^2 during hydrothermal alteration. If substantial vapor volumes are required for soil alteration, the permeability must exceed 10^{-15} m^2. The principal application of our model is to test the viability of hydrothermal circulation as the primary process responsible for the broad spatial correlation of Martian valley networks with magnetic anomalies. For host rock permeabilities as low as 10^{-17} m^2 and intrusion volumes as low as 50 km^3, the total discharge due to intrusions building that part of the southern highlands crust associated with magnetic anomalies spans a comparable range as the inferred discharge from the overlying valley networks. *INDEX TERMS:* 1832 Hydrology: Groundwater transport; 1860 Hydrology: Runoff and streamflow; 1545 Geomagnetism and Paleomagnetism: Spatial variations (all harmonics and anomalies); 5440 Planetology: Solid Surface Planets: Magnetic fields and magnetism; 5114 Physical Properties of Rocks: Permeability and porosity; *KEYWORDS:* Hydrothermal, groundwater, runoff, crustal magnetism, intrusions

1. Introduction

[2] Hydrothermal circulation is an important part of many terrestrial igneous, metamorphic, and sedimentary environments and has profound geochemical and biological implications. On the Earth it accelerates the cooling of magmatic bodies in systems ranging from divergent plate boundaries to individual volcanoes and frequently produces discharge in the form of hot springs, geysers, and submarine vents. There is also evidence for the past existence of hydrothermal systems on Mars (see *Farmer* [1996] for a review). Valley networks are associated with structures that are able to force groundwater to the surface [*Baker et al.*, 1992]; these include some of the younger volcanoes [*Gulick*, 1998], ancient volcanoes, rifts, and impact craters [*Tanaka et al.*, 1998]. Many more observations have led to groundwater discharge as the favored method of runoff production (see *Baker et al.* [1992], *Baker* [2001], and *Carr* [1996] for reviews) [*Malin and Carr*, 1999; *Malin and Edgett*, 2000]. Hydrothermal circulation may also have altered the Martian crust and further produced weathering products and soil [*Griffith and Shock*, 1997; *Newsom et al.*, 1999]. The greatest consequence of hydrothermal activity on Mars may be its ability to sustain life [*Shock*, 1996; *Farmer*, 1996].

0148-0227/02/2001JE001616S09.00

[3] We present here numerical models of the thermal convection of groundwater in a porous host rock due to the presence of an intruded magma chamber. An extensive portion of the available parameter space is explored in order to quantify the effects that magma chamber volume, depth, aspect ratio, and host rock permeability and porosity have on surface discharge. The results of this general approach are then applied to some specific issues. First, we use geochemical constraints to bound the permeability of the Martian crust. Second, we test the hypothesis that hydrothermal circulation can explain the putative correlation observed between valley networks and magnetic anomalies [*Jakosky and Phillips*, 2001]. We suggest that large amounts of water were circulated throughout the southern-highlands crust due to magmatic intrusion and that the portion of this water discharged to the surface can quantitatively account for the valley networks preserved since the end of crustal formation.

2. Model

[4] Two-dimensional, axisymmetric representations of hydrothermal circulation in a magma chamber and its host rock were modeled with the U.S. Geological Survey (USGS) code HYDROTHERM [*Hayba and Ingebritsen*, 1994, 1997] and its graphical user interface HTpost (P. S. Hsieh, USGS, unpublished material, 2000). HYDROTHERM can model temperatures from about 0° to 1200°C and pressures from 0.5 to 10,000 bars and keeps track of both liquid

and gaseous phases of pure water. It solves mass, momentum, and energy balance equations expressed in terms of dependent variables pressure and enthalpy. The choice of enthalpy over temperature allows the thermodynamic state of the fluid to be specified uniquely under two-phase conditions. Viscosity and density for a particular temperature and pressure are obtained from a look-up table.

[5] The momentum balance equation is Darcy's law, which for a single fluid phase i is

$$\mathbf{v}_i = -\frac{k^i_{\mathrm{rel}} k}{\mu_i}(\nabla p + \rho_i g \nabla z), \tag{1}$$

where $\mathbf{v}_i$ is the Darcy velocity, k is intrinsic permeability, μ_i is dynamic viscosity, p is pressure, ρ_i is density, g is gravitational acceleration, and z is depth. The relative permeability k^i_{rel} quantifies the reduction of the flow of phase i due to the presence of the other phase. The mass balance (continuity) equation for phase i is

$$\frac{\partial}{\partial t}(nS_i\rho_i) + \nabla \cdot (\rho_i \mathbf{v}_i) = 0, \tag{2}$$

where n is porosity, t is time, and S_i is volumetric saturation ($S_{\mathrm{water}} + S_{\mathrm{steam}} = 1$, i.e., the medium is fully saturated). The continuity equation for the entire system is the sum of the equations for each phase. The energy-balance equation for the entire system is

$$\frac{\partial}{\partial t}\left[(1-n)\rho_r h_r + n\sum_i S_i\rho_i h_i\right] + \nabla \cdot \left[\sum_i k_{ri}\rho_i h_i \mathbf{v}_i\right] - \nabla \cdot K_m \nabla T = 0 \tag{3}$$

where h is enthalpy, T is temperature, K_m is medium thermal conductivity, and subscript r refers to rock matrix properties. HYDROTHERM solves the equations by performing Newton-Raphson iterations on an equivalent finite difference system (with the horizontal dimension expressed in radial coordinates) until mass and energy residuals fall below specified maximum values.

[6] The horizontal extent of the host rock is 20 times that of the magma chamber and the vertical extent is 20 km, both of which are sufficient to accommodate flow from all magma chambers studied. The right vertical boundary is not intended to represent the limit of a horizontally bounded water source, but to provide enough space for a realistic response to a local temperature perturbation. As much fluid flows through this boundary as is necessary to balance the net flow through the top horizontal boundary. The suitability of the chosen horizontal extent was tested by a baseline model measuring 40 chamber radii across, which yielded almost the identical discharge to the original model. Fluid is allowed to cross the upper horizontal and right vertical boundaries, while temperature and pressure are fixed. Recharge from the surface is typically <10% of discharge, indicating that the strength of discharge does not depend on infiltration of runoff. Adaptive boundary conditions to prevent infiltration for a dry Mars could therefore be neglected. Sufficient recharge or discharge occurs through the right vertical boundary to conserve the mass of the system.

[7] The initial pressure distribution is hydrostatic, with a surface value of 1 bar. A small geothermal gradient (0.5°C/km), applied to ensure stable decay of the surface discharge, does not otherwise affect the model (the effects of substantial geothermal gradients were explored, and the results are described below). The lowest temperature HYDROTHERM can handle in this model is 10°C, and this was used for the surface boundary condition. Both the surface temperature and pressure were adopted for numerical convenience, and they neither affect the results nor are intended to represent Earth-like climatic conditions. The left vertical and lower horizontal boundaries are no-flow, and the temperature and pressure are free to vary. Grid spacing is ~100 m in both directions near the magma chamber and at greater horizontal distances increases logarithmically.

[8] Present Martian conditions may include a permafrost layer which must first be melted before discharge is produced. *Gulick* [1998] estimated that the time required to melt a 2 km thick layer of permafrost was much less than the lifetime of the hydrothermal system, making it unlikely that quantities integrated over the lifetime of the system, such as total discharge, should be significantly altered. During the late Noachian, when the hydrothermal systems proposed here were active, the permafrost layer was likely to be much thinner than 2 km, making melting times even shorter. A HYDROTHERM simulation that quantifies the role of ice in our models is described below.

[9] Our baseline model consists of a 50 km^3 chamber emplaced at a depth of 2 km below the surface into host rock of permeability 10^{-16}m^2. The dimensions of the chamber are expressed in terms of its aspect ratio (D/H), defined here as the ratio of diameter to height. The baseline chamber has $D/H = 2$. The volume of the chamber is taken after that modeled by *Hayba and Ingebritsen* [1997] and is also of similar size to magma chambers found under mid-oceanic ridges [*Burnett et al.*, 1989]. Note that our baseline model is intended only as an example model from which we later deviate extensively and does not necessarily represent any sort of "ideal" parameter values.

[10] The chamber is emplaced instantaneously at a temperature of 900°C. Because this approach ignores discharge produced during supersolidus cooling and the finite intrusion process, it produces relatively conservative results. The magma chamber is initially impermeable, but as it cools through a brittle-ductile transition (BDT) between 400° and 360°C, it is assumed to fracture and become as permeable as the surrounding host rock [*Hayba and Ingebritsen*, 1997]. A semilog form is adopted for this transition, wherein the log of the permeability scales linearly with temperature. Note that the "permeability" BDT may differ somewhat from the classic "deformational" BDT [e.g., *Kohlstedt et al.*, 1995]. All models use a rock density of 2500 kg m^{-3}, a thermal conductivity of 2.0 W m^{-1} K^{-1}, and a porosity of 1%. Deviations from the baseline model include host rock permeabilities of 10^{-17} and 10^{-15} m^2, porosity of 25%, magma chamber aspect ratios of 0.2 and 20, depths of 8.5 and 15 km, and volumes of 100 and 2000 km^3.

[11] Steam and water fluxes, while fundamental to discharge calculations, may also be used to test hypotheses regarding the possible geochemical alteration in the system. For each time step, a measure of water-to-rock ratio for reactions above a particular temperature threshold may be calculated by measuring the total mass of water that passes through the region warmer than the threshold value and dividing by the volume of the region.

3. Results

[12] In the baseline model (magma chamber depth is 2 km, volume is 50 km^3, $D/H = 2$, and host rock permeability is 10^{-16} m^2; Figure 1) an initial peak in the surface discharge occurring at only a few hundred years following magma emplacement is due to thermal pressurization [*Delaney*, 1982]. Its peak value is not significantly greater than discharges that occur later in the model. The extremely short-lived nature of this effect, which is less extreme for higher host rock permeabilities, contributes negligibly to the total, time-integrated mass of water produced by the system (total discharge), which we assume to be of primary importance in valley erosion. Additionally, thermal pressurization may be weaker in the more realistic case of a finite duration intrusion process.

[13] The broad peak at 45 kyr is due to thermal convection of groundwater. At first, the chamber is supercritical and impermeable, allowing convection in the surrounding host rock only. Surface discharge peaks when the magma chamber has cooled sufficiently to become permeable and admit advection. When only

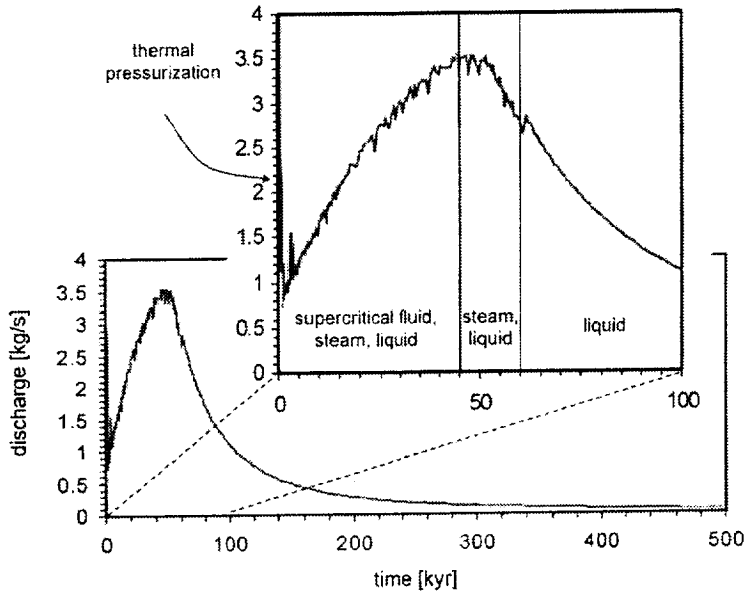

Figure 1. Surficial discharge from the baseline model (magma chamber depth 2 km, volume 50 km^3, aspect ratio 2, host rock permeability 10^{-16} m^2). The regions separated by solid vertical lines in the enlarged portion of the figure denote the different phases present within in the model. The magma chamber becomes permeable over the interval 0.7–57 kyr. The noise on the curve is due mainly to discretization effects in the presence of steam, which has much greater velocity than the liquid phase.

the liquid phase remains, the exponential decay of discharge becomes much smoother and dies out at about 2.8×10^6 years.

3.1. Permeability

[14] For simplicity, permeability was homogeneous in all models. *Gulick* [1998] used a value of 10^{-11} m^2 for hydrothermal systems on Mars inferred from young, near-surface Hawaiian volcanics. *Ingebritsen and Sanford* [1998], however, report that permeabilities in the east rift zone at Kilauea, while high near the surface (10^{-10}–10^{-9} m^2), are much lower at depths of just 1–2 km (10^{-16}–10^{-15} m^2) in rock of the same composition. *Manning and Ingebritsen* [1999] estimate values of between 10^{-17} and 10^{-14} m^2 for the mean continental permeability between 1 and 10 km depth. We modeled permeabilities from 10^{-17} to 10^{-15} m^2 (Figure 2). The upper limit is for computational convenience; we demonstrate below that results for higher permeabilities can be extrapolated from this range.

[15] Discharge from the low-permeability (10^{-17} m^2) model has a characteristically large thermal pressurization peak followed by a weak main peak. Conduction is the dominant mode of heat transfer in this model, and the spatially integrated surface discharge at any given time (henceforth called "instantaneous discharge") is only about a tenth that of the baseline model. In the baseline model, convection and conduction play comparative roles in heat transport, while in the high-permeability (10^{-15} m^2) model, convection is dominant. Discharge in all three models lasts between 2500 and 3000 kyr, but rate of decay of discharge is, in general, proportional to permeability, with the 10^{-17} m^2 model decaying to a tenth of its peak value in 200 kyr, the baseline model in 175 kyr, and the 10^{-15} m^2 model in 135 years.

[16] An important feature of the $k = 10^{-15}$ m^2 model is the presence of a steam-dominated zone above the magma chamber during the first several thousand years. This phenomenon may have implications for chemical alteration, as described in the discussion below.

[17] The relationship of discharge to permeability was investigated using the high-permeability results of *Gulick* [1998] as a starting point. She modeled a 10^{-11} m^2 hydrothermal system which included the magma chamber implicitly through a heat flux boundary condition based on the analytical solution to the conductive heat flow through the wall of an infinitely long cylinder. This implies that no heat was lost through the roof and floor of the

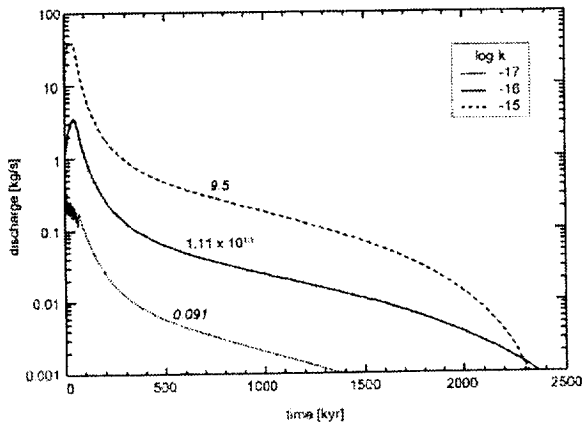

Figure 2. Surficial discharge from a 2 km deep magma chamber of volume 50 km^3 for host rock permeabilities of 10^{-17}, 10^{-16}, and 10^{-15} m^2. The total discharge of the $k = 10^{-16}$ m^2 model, in kilograms, appears above its curve. The numbers above the other curves denote the fraction of this discharge that their corresponding models produced.

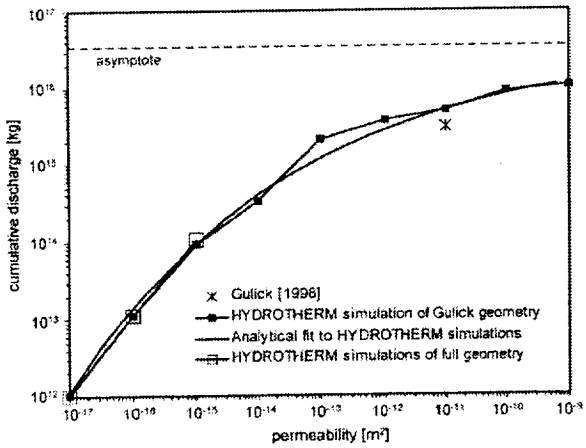

Figure 3. Discharge results from HYDROTHERM models of a geometry similar to those of *Gulick* [1998]. An analytic fit to these data, with its large permeability asymptote, is shown. The discharge obtained by the single permeability modeled by Gulick is provided for comparison, as are the total discharges of our three full geometry models (from Figure 2). The value obtained by Gulick was converted from volume to mass for the purpose of this figure, with an assumed water density of 1000 kg m^{-3}.

chamber and that no BDT was encountered on cooling. By adopting these limitations in HYDROTHERM, the problem is more efficient numerically and allows us to extend the range of assumed permeability (Figure 3) and to compare the results directly to those of *Gulick* [1998]. Our results agreed fairly well, although a small difference resulted owing to our more realistic magma chamber heat flux and possibly other factors such as numerical solution. Overall, we found that the relationship between total discharge and permeability could be represented approximately by

$$D = a - be^{-cK}, \tag{4}$$

where D and K are the base 10 logarithms of total discharge and permeability, respectively, and a, b, and c are positive constants (with best fit values of 38, 0.089, and 0.12, respectively). As $K \rightarrow \infty$, $D \rightarrow a$, meaning that as permeability tends to very high values, discharge increases asymptotically toward a finite maximum value. This is not surprising, since the forces driving the flow are limited by the amount of heat contained in the magma chamber. For the range of permeabilities covered with our own, more complete geometry ($K < -15$), D is approximately linear in K. Note that the total discharges (whose relative magnitudes are given above each curve in Figure 2) exhibit this linear behavior.

[18] For our range of permeabilities, total discharge is approximately the same for both geometries. At higher magma chamber aspect ratios, however, it is no longer reasonable to assume that heat is lost through the chamber walls alone, and the total discharges for the two geometries are expected to diverge. Instantaneous discharge is not the same for both geometries, even with $D/H = 2$. Our geometry produces a greater maximum than the simpler geometry (~1.75 times as high for $k = 10^{-16}$ m^2) but drops more rapidly thereafter.

[19] Magma chamber cooling times, defined here as the average time taken for chamber nodes to cool below a specified threshold temperature, are of interest in these models. For all three permeabilities the cooling time for a threshold of 450°C (i.e., half the emplacement temperature) is ~30 kyr. While an increase in host rock permeability increases the velocity of the flow alongside the still impermeable magma chamber, it does not significantly enhance cooling [see *Norton and Knight*, 1977]. Once the chamber becomes permeable, however, cooling progresses as different rates in each model. The time taken for the chamber to cool to 250°C was 67, 61, and 40 kyrs for permeabilities of 10^{-17}, 10^{-16}, and 10^{-15} m^2, respectively.

3.2. Volume

[20] *Head and Wilson* [1994] suggest that Martian magma reservoir volumes could be as great as 2000 km^3 and that chamber depths are most likely to range from 8 to 12 km. We ran models of $D/H = 2$ magma chambers with volumes of 100 and 2000 km^3 at a depth of 8.5 km and with host rock permeability of 10^{-16} m^2 (Figure 4). The 100 km^3 chamber produced ~2.5 times as much discharge as the 50 km^3 chamber, while the jump from 100 to 2000 km^3 resulted in a factor of 73 increase. This approximately linear relationship is reflected in the magnitude of the instantaneous discharge, whose peak value has proportional increases. This, coupled with an increase in cooling time with volume (and therefore an increase in the discharge lifetime), explains the observed total discharge increase.

[21] Although not obvious on the semilog plot of Figure 4, the discharge produced by the 2000 km^3 chamber drops off at ~800 kyr, which is in agreement with values obtained by *Cathles et al.* [1997] for a 2500 km^3 chamber with host rock permeabilities ranging from 4×10^{-17} to 10^{-16} m^2.

3.3. Depth

[22] Models with 50 km^3 magma chambers at depths of 8.5 and 15 km and with host rock permeability of 10^{-16} m^2 were run (Figure 5). Total discharge decreases by a factor of ~1.5 with each 6.5 km increase in depth. Similar depth dependence exists for the same three chamber depths at host rock permeabilities of 10^{-17} and 10^{-15} m^2. A summary of the total discharge of all nine depth and permeability combinations is depicted in Figure 6. The very small geothermal gradient in these models makes magma chamber cooling times only marginally sensitive to changes in depth. All three chambers cool to half their emplacement temperature (450°C) in ~30 kyr. The 2 km deep chamber cools to 250°C in 61 kyr, while the 15 km chamber takes 71 kyr. Flow from deeper chambers must

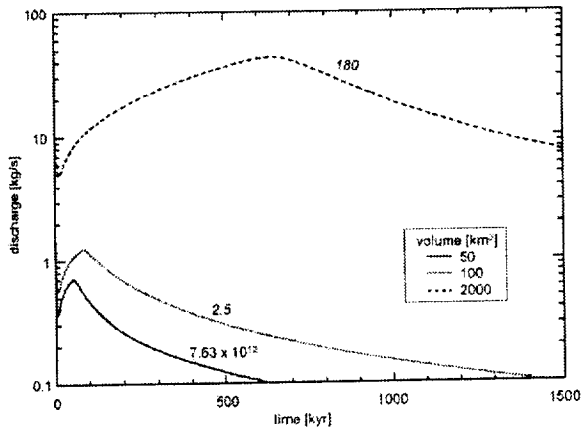

Figure 4. Surficial discharge from magma chambers of volume 50, 100, and 2000 km^3, all at a depth of 8.5 km, an aspect ratio of 2, and with host rock permeability of 10^{-16} m^2. The total discharge of the 50 km^3 model appears above its curve. The numbers above the other curves denote the fraction of this discharge that their corresponding models produced.

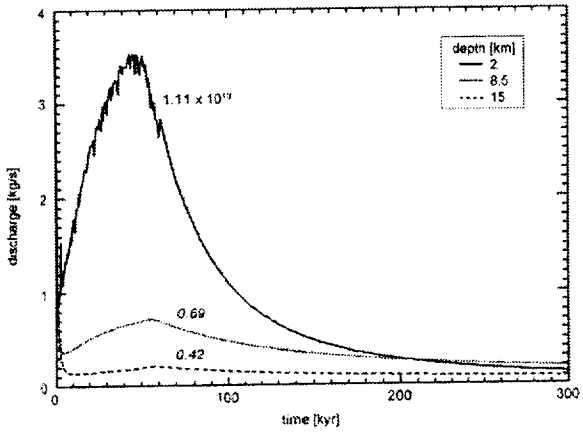

Figure 5. Surficial discharge from 50 km^3 magma chambers at depths of 2, 8.5, and 15 km, all with aspect ratio 2, and with host rock permeability of 10^{-16} m^2. The total discharge of the 2 km deep chamber appears above its curve. The numbers above the other curves denote the fraction of this discharge that their corresponding models produced.

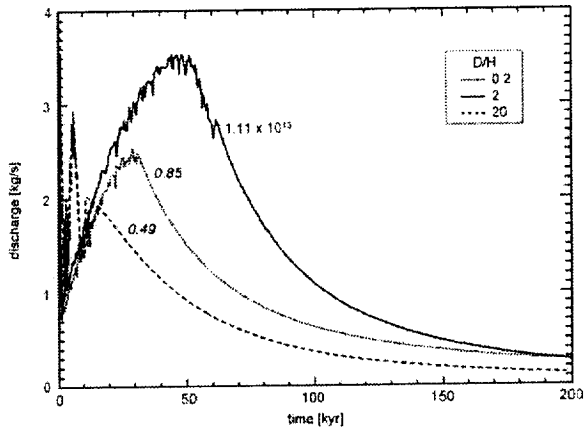

Figure 7. Surficial discharge from 50 km^3 magma chambers with D/H = 0.2, 2, and 20, all at a depth of 2 km, and with host rock permeability of 10^{-16} m^2. The total discharge at D/H = 2 appears above its curve. The numbers above the other curves denote the fraction of this discharge that their corresponding models produced.

travel farther in order to expel heat from the system and is therefore less efficient at cooling the magma chamber.

3.4. Aspect Ratio

[23] Magma chambers with D/H = 0.2, 2, and 20 were modeled (Figure 7). These correspond to chamber radii of 1.2, 2.5, and 5.4 km and chamber heights of 12, 2.5, and 0.54 km. Chamber depth in all cases is 2 km, and chamber volume is 50 km^3. The horizontal extent was fixed at 50 km for all three models, rather than scaled with the chamber radius, so that the influence of the right vertical boundary was the same in each model. The total discharge of these models is controlled by the cooling time of the magma chamber, and therefore its surface area/volume ratio A/V (1.89, 1.59, and 4.06 km^{-1} for the three aspect ratios, respectively). There is an approximately linear inverse relationship between A/V and total discharge; that is, high A/V implies low total discharge and vice versa. The effects of aspect ratio are observed more directly when a substantial geothermal gradient is applied (see section 3.5).

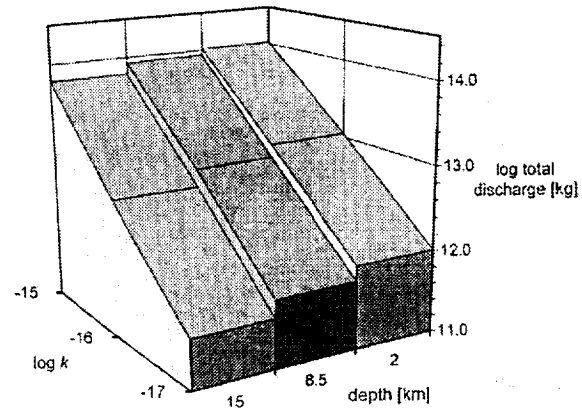

Figure 6. Total discharge from 50 km^3 magma chambers of aspect ratio 2 at depths of 2, 8.5, and 15 km and host rock permeabilities of 10^{-17}, 10^{-16}, and 10^{-15} m^2.

[24] In all three models the flow pattern consists of a single, clockwise rotating convection cell alongside the chamber. For D/H = 20 this pattern does not give way to a series of cells above the chamber roof, as one might expect for flow between two infinite horizontal surfaces at different temperatures.

3.5. Geothermal Gradient

[25] Models with magma chamber aspect ratios of 0.2, 2, and 20 were run with an initial host rock geothermal gradient of 20°C/km, perhaps representative of early Mars [*Schubert et al.*, 1992]. The presence of a geothermal gradient significantly affects the hydrothermal discharge. The flat, sill-like chamber (D/H= 20) produces the greatest peak discharge because of its large horizontal exposure. The discharge dissipates more rapidly, however, because the chamber, having the greatest A/V and being oriented perpendicular to the main flow direction, cools rapidly. Conversely, the tall, pipe-like chamber (D/H = 0.2), being immersed in warmer temperatures at depth, cools more gradually. Its geometry produces the largest convection cell and offers minimum obstruction to flow, resulting in the greatest total discharge despite its low peak value. Overall, tenfold variations in aspect ratio produce changes in discharge of less than a factor of 3.

[26] The effect of geothermal gradient is also observed in cooling times. The times taken for magma chambers to cool to half their emplacement temperature are, in order of increasing aspect ratio, 25, 45, and 4.0 kyr, respectively. In the absence of a significant geothermal gradient, the same chambers cool in 16, 28, and 3.5 kyr, respectively. An 8.5 km deep chamber in a geothermal gradient of 20°C/km cools to half its initial temperature in 52 kyr (as opposed to 30 kyr for the model with negligible geotherm). It also produces ~7 times as much discharge (with a peak 3.5 times higher) as the identical model with a negligibly small geothermal gradient.

[27] It should be noted that for permeabilities >10^{-16} m^2, the Rayleigh number of a plane porous medium [e.g., *Turcotte and Schubert*, 1982] at 20°C/km indicates that weak convection may occur in the absence of a magma chamber. This phenomenon is observed in our high geothermal gradient models when no magma chamber is emplaced. Free convection in the terrestrial crust has been invoked by *Raffensperger and Garven* [1995] to explain the location of uranium ore deposits in sedimentary basins in Canada and Australia. *Travis et al.* [2001] showed that free convection may be capable of melting significant volumes of subsurface ice in the

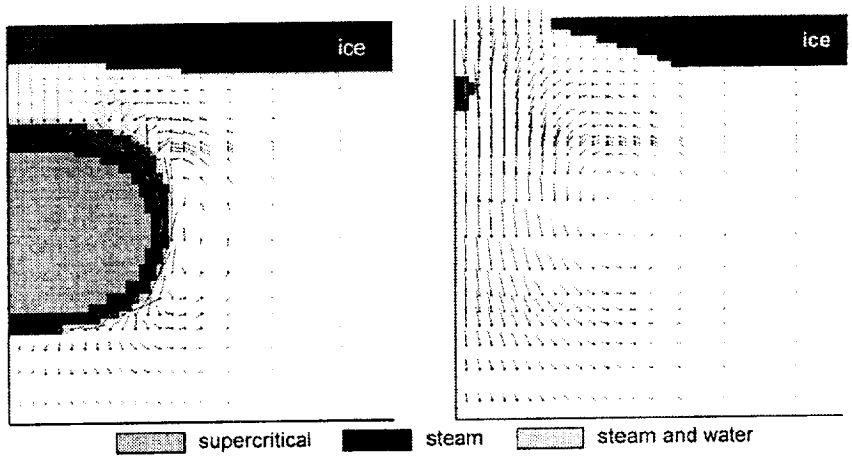

Figure 8. Baseline model with an initially 1 km thick subsurface ice layer shown at (left) 15 kyr and (right) 59 kyr. Both horizontal and vertical dimensions in each image are approximately 5 km. Water and steam velocities are shown by black and gray streamers, respectively. Only every other row and column are shown. Shaded regions (apart from the ice) represent different fluid phases as described in the key. At 59 kyr, only a small remnant of steam remains, and the magma chamber has become as permeable as the host rock.

Martian crust. However, all of these models, including our own, have homogeneous permeability in the convecting zone: realistic vertical heterogeneity in planetary crusts will both inhibit the development of large-scale crustal convection and decrease the efficiency of heat transfer. Although background geothermal gradients may affect cooling times of intrusions, we view their contribution to hydrothermal circulation as doubtful.

3.6. Ice

[28] *Gulick* [1998] suggested that a 2 km thick subsurface permafrost layer above a 50 km^3 magma chamber would melt in a few tens of thousands of years. This is of the same order as the time taken for discharge to peak in our own models, indicating that ice could significantly reduce total discharge. We thus ran the baseline model with a 1 km thick layer of subsurface ice (Figure 8), modeled after *Bonacina et al.* [1973], who approximated the melting process as a cooling period over a small finite temperature interval ΔT. During melting the material is assigned an augmented specific heat given by

$$C_S = C_L + \frac{L}{\Delta T},$$

where subscripts S and L refer to the solid and liquid phases, respectively, and L is the latent heat of fusion. We used $c_L = 1000$ J kg^{-1} K^{-1}, $L = 3.34 \times 10^5$ J kg^{-1}, and $T = 5°C$, giving $c_L = 6.78 \times 10^4$ J kg^{-1} K^{-1}.

[29] The hydrothermal system took 52 kyr to melt a hole in the ice. The strong upward convection associated with increasing magma chamber permeability did not noticeably increasing melting rate. The total discharge produced by the model was 2.95×10^{11} kg, about a quarter that of the baseline model. This relatively severe reduction (which is expected to be worse for deeper chambers and lower host rock permeabilities) places an upper bound on permafrost thickness during valley formation on Mars. For valleys to form through sapping processes alone, the permafrost must be melted through, or aquifers carrying groundwater beneath the permafrost must intersect the surface. In either case, the permafrost can be no thicker than a few hundred meters.

3.7. Water Table

[30] Surface discharge will occur only if convection is strong enough to elevate groundwater from the initial water table depth to the surface. We compared with hydrostatic conditions the vertically integrated product of density, gravitational acceleration, and depth in order to estimate the height a water table may attain through thermal-convective expansion. Integrations were performed over all vertical columns of finite difference blocks at all times and for a

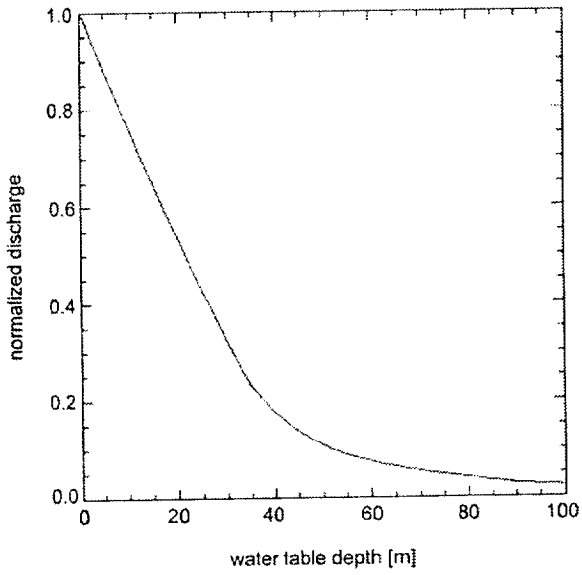

Figure 9. Discharge as a function of water table depth, normalized to the zero depth water table value.

Table 1. Water/Rock Ratios by Mass Calculated for 8.5 km Deep Chambers of the Indicated Volumes and Host Rock Permeabilities k

Threshold Temperature, °C	$k = 10^{-15}$ m^2 Volume = 50 km^3	$k = 10^{-16}$ m^2 Volume = 50 km^3	$k = 10^{-16}$ m^2 Volume = 2000 km^3
150	0.12	0.025	0.067
200	0.18	0.037	0.10
250	0.28	0.054	0.15

range of water table depths. The discharge was calculated from those parts of the water table that intersected the surface and was compared to zero depth water table models. The results (Figure 9) show that models with a water table 50 m deep produce only 10% of their zero depth water table equivalents, while models with a 100 m deep table produce only 2%.

4. Discussion

4.1. Implications for Hydrothermal Alteration

[31] Water/rock ratio (*W/R*) can be an important influence on the mineralogy of alteration products in hydrothermal systems. Martian hydrothermal alteration is thought to occur at low *W/R* (<10 by mass) [*Griffith and Shock*, 1997; *Newsom et al.*, 1999], in which case its effect is small, and the initial mineral composition is the primary influence on the alteration assemblage [*Griffith and Shock*, 1997].

[32] HYDROTHERM mass flux results allow the *W/R* of a hydrothermal model to be calculated. At each time step, regions of the model above a specific threshold temperature are identified, and the total flux passing through them is calculated. On the basis of these data, a *W/R* (by mass) is calculated for each finite difference block in the model that is at some time above the threshold temperature. The average *W/R* values for the three reaction temperatures modeled by *Griffith and Shock* [1997], and for various model dimensions, are shown in Table 1.

[33] The large velocities in the $k = 10^{-15}$ m^2 model give the highest *W/R* for all threshold temperatures, ~5 times that of the $k = 10^{-16}$ m^2 model with a chamber of the same volume. Negligible geothermal gradient and low host rock permeability in our models are both factors that contribute to small *W/R*. Typical Martian geotherms (>50°C/km) will lead to larger *W/R*, so these estimates can be viewed as lower bounds. The presence of a significant geotherm may be expected to increase discharge by a factor of about 3 or 4 (as observed in the model with an 8.5 km deep chamber with geothermal gradient), and since *W/R* is directly proportional to the discharge flowing through the alteration area, it may experience a similar increase. This would still leave most values listed in Table 1 below unity.

[34] A primary goal of the work by *Griffith and Shock* [1997] was to calculate the amount of water bound to the rock during alteration. In a model based on the Shergotty SNC meteorite, ~8% of the final mineral assemblage (by weight) was water, implying that water/rock ratios >0.08 would be necessary to sustain hydrothermal circulation. Assuming the Shergotty composition is sufficiently generic to be applied to our own models, a *W/R* limit of 0.08 implies a minimum permeability of 10^{-16} m^2 for a 150°C reaction in host rock surrounding a 2000 km^3 chamber (Table 1).

[35] *Newsom et al.* [1999] suggest that the relative abundances of mobile elements such as sulfur, chlorine, sodium, and potassium may be explained by the presence of a mixture of neutral-chloride and acid-sulfate fluids during soil formation. Production of the latter fluid requires vapor transport [*Rye et al.*, 1992], and *Ingebritsen and Sorey* [1988] discuss situations in which vapor-dominated zones may occur. Their models require combinations of low-permeability barriers and in some instances topographic gradients to sustain vapor-dominated zones, which develop in the shallow subsurface only. These specialized structures have not been included in our generalized models; nonetheless, our highest permeability model (10^{-15} m^2) with the shallowest chamber (2 km) does produce a short-lived (few thousand years) two-phase zone between magma chamber and surface. Steam develops here because of a combination of low pressures (which drop to a

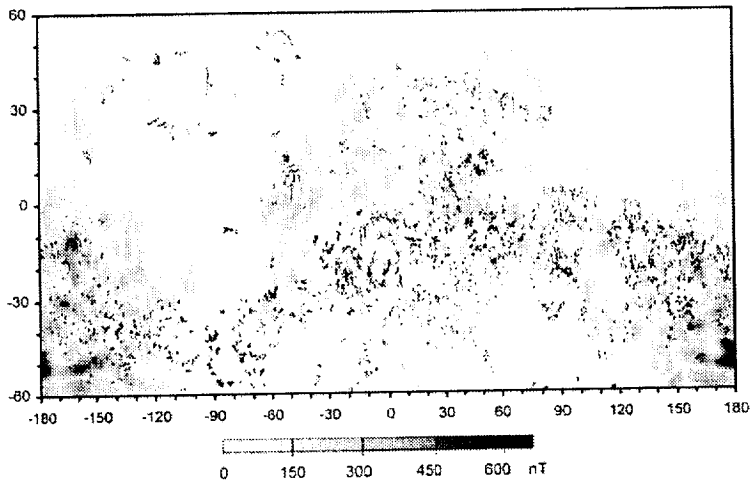

Figure 10. Overlay of the absolute values of the 200 km vertical magnetic anomalies [*Purucker et al.*, 2000] and the valley networks [*Kieffer*, 1981] (cylindrical projection). Valleys were not mapped for latitudes below 60°S. The anomalies range from 0 to 670 nT.

Table 2. Statistical Data for the Correlation Between Valley Networks and Magnetic Anomalies

Magnetic Threshold, nT	p_0	p	$(p - p_0)/p$	Q			
				$d_m = 2°$	$d_m = 3°$	$d_m = 4°$	$d_m = 6°$
1	0.896	0.962	0.069	0.0785	0.182	0.494	0.464
2	0.827	0.928	0.109	0.0204	0.102	0.210	0.654
5	0.669	0.827	0.191	0.00228	0.0480	0.172	0.268
10	0.469	0.658	0.287	0.00223	0.0345	0.160	0.434
20	0.295	0.465	0.366	0.00459	0.0590	0.166	0.343
50	0.126	0.201	0.373	0.0686	0.303	0.330	0.612
100	0.0521	0.0818	0.363	0.260	0.450	0.575	1

minimum of about two thirds hydrostatic pressure) and high temperatures. At lower permeabilities, fluid rising from the chamber does not transport enough heat upward to elevate temperatures to the required levels for steam production.

[36] If substantial quantities of vapor are required for soil alteration, then the abundance of steam in our high-permeability model may point to 10^{-15} m^2 as a lower bound to permeability, a somewhat tighter constraint than that imposed by W/R ratio alone. Alternatively, if volcanic aerosols [*Newsom et al.*, 1999] or basalt palagonitization [*McSween and Keil*, 2000] produce sufficient soil alteration, then no such limit is necessary.

4.2. Relationship of Hydrothermal Circulation to Valley Networks and Magnetic Anomalies

[37] The apparent spatial correlation between valley networks and magnetic anomalies suggests a link between processes involving the acquisition of thermoremnance in a cooling intrusion and processes involving the production of surface water for the creation of fluvial channels, i.e., hydrothermal circulation. An overlay of maps (Figure 10) showing the valley networks [*Kieffer*, 1981] and the vertical component of the magnetic anomalies as measured by the Mars Global Surveyor magnetometer [*Acuña et al.*, 1999] inferred at a constant altitude of ~200 km [*Purucker et al.*, 2000] visually suggests that the two are correlated [*Jakosky and Phillips*, 2001].

[38] A statistical analysis of the relative positions of valley networks and magnetic anomalies quantifies the correlation. A binomial test was performed, with success defined as the occurrence of a valley network and a magnetic anomaly (with vertical component above a specified threshold) in the same data bin. We consider only the southern highlands in these calculations. The valley network map [*Kieffer*, 1981] contains the coordinates of the 0.25 by 0.25 degree bins that contain valleys; the number and length of the valleys are not quantified. The magnetic anomaly map [*Purucker et al.*, 2000] is binned at 1 by 1 degree and was regridded at 0.25 degree to match the valley grid. The number of degrees of freedom must, however, be adjusted to match the true spatial resolution, which is limited by the magnetic data. The total number of 0.25 degree bins is therefore multiplied by the quantity

$$\varepsilon = \left(\frac{0.25}{d_m}\right)^2,$$

where d_m is the length scale in degrees for magnetic resolution. We determined that the variogram for the 200 km magnetic field reaches half of its sill (asymptotic) value in 200 km and 90% of the sill value in 400 km, in agreement with the rule of thumb for potential fields that the spatial resolution is approximately equal to measurement altitude. Therefore $d_m \sim 200$ km (~3 degrees) may be most appropriate, but we consider a range from 2 to 6 degrees.

[39] Relevant probabilities may be obtained using the total number N of 0.25 by 0.25 degree bins in the region of interest, the number n of these bins containing valleys, the number m of bins with magnetic anomalies above a specified threshold, and the number C of correlations. The observed correlation probability is then $p = C/n$, while the expected correlation probability for a valley placed randomly in the region of interest is $p_0 = m/N$. The probability q of obtaining C or more correlations if the n valleys are placed randomly in the region of interest can be obtained using the cumulative binomial distribution with εC, εn, and p_0 as the minimum number of successes, the number of independent trials, and the probability of a single success, respectively. A low value of q implies that the relative distribution of valleys and magnetic anomalies on Mars is not what one would expect from chance.

[40] The results for a range of magnetic anomaly thresholds (Table 2) indicate that minimum chance probabilities occur near a 10 nT threshold for the vertical magnetic field at 200 km altitude. The area containing magnetic anomalies falls off sharply at higher thresholds, allowing a greater probability of chance correlation. At lower thresholds the entire map is considered anomalous, and so again it is easier to produce randomly the observed correlation. Over length scales at which the magnetic anomalies can be described as strongly coherent ($d_m < 4$ degrees), the probability of a chance correlation is relatively small ($q < 0.16$).

[41] A genetic correlation requires that the valley networks and magnetic anomalies are the same age. A significant majority of valleys are Noachian (70–92% [*Scott and Dohm*, 1992; *Carr*, 1996]); many of those that are younger are not in the southern highlands and so are excluded from our survey. The magnetic anomalies, because of their inferred deep-crustal origin (see proposition 1 below) without surface manifestation, must also be very old. However, even the oldest valley networks individually preserve only some part of the Noachian that was not subsequently locally erased, whereas the magnetic anomalies probably reflect a greater span of crustal history. In other words, some valley networks that were associated with magnetic anomalies may have been resurfaced, whereas other valley networks may have formed subsequent to emplacement of the magnetic anomalies by hydrothermal or other processes. The normalized excess of correlated valleys and magnetic anomalies $(p - p_0)/p_0$ (Table 2) may be taken as representative of the fraction of valleys for which a genetic correlation may be inferred, between about one quarter and one third.

[42] The role of hydrothermal circulation in the relationship between valley networks and magnetic anomalies may now be described in terms of a central hypothesis composed of two main propositions, defined and discussed in the following sections.

4.2.1. Proposition 1. [43] The first proposition is that the magnetic anomalies formed as intruded crust and that the acquisition of thermal remnant magnetization (TRM) occurred at relatively great depth. The strong observed magnetizations in the Martian crust of 20–40 A m^2 [*Connerney et al.*, 1999; *Grimm*, 2000] imply magnetization depths of up to a few tens of kilometers. The presence of magnetic anomalies in Arabia Terra, which has been strongly resurfaced [*McGill*, 2000; *Hynek and Phillips*, 2001], also points to a deep origin. On Earth, Layer 3 gabbros of the oceanic crust are magnetized to the extent that they contribute between 25 and 75% of the observed marine anomalies [*Pariso and Johnson*, 1993], while the underlying mantle is unmagnetized [*Wasilewski et*

al., 1979]. Therefore deep crustal magnetization of Mars is reasonable.

[44] The mineral composition of the magnetized material producing the magnetic anomalies is likely to contain magnetite or hematite as the primary magnetic carrier. Although magnetite is generally favored, there is much support for hematite [e.g., *Connerney et al.*, 1999]. *Kletetschka et al.* [2000] show that for an applied magnetic field of 0.1 mT (about twice the strength of the Earth's present geomagnetic field), multidomain hematite reaches maximum TRM saturation, whereas magnetite reaches only a few percent thereof.

4.2.2. Proposition 2. [45] The second proposition is that hydrothermal discharge attending crustal formation processes in the southern hemisphere of Mars was sufficient to provide the water necessary to carve the valley networks. We assume that where instantaneous discharges predicted by our models are too small to do significant geomorphic work, topographical variations and near-surface heterogeneity in the host rock permeability (especially in the horizontal dimensions) are sufficient to concentrate discharge to the required levels. Hydrothermal systems on Earth exhibit such discretized concentration of outflow, as evidenced by the presence of geysers and springs rather than diffuse outflow everywhere above the magmatic intrusion. The Martian valley networks are characterized by low drainage densities, implying again that crustal heterogeneities may localize discharge.

[46] Testing this proposition requires knowledge of the amount of water necessary to erode the valley networks, the total amount of water available to hydrothermal systems, and the actual hydrothermal discharge produced. An estimate of the required water volume for valley erosion may be made from values of areal coverage, drainage density, valley cross section, and sediment-to-water ratio. Using a map of drainage densities [*Carr and Chuang*, 1997], we estimate the total area covered by valley networks to be about 1.4×10^7 km^2. Since we estimated earlier that only one quarter of the valley networks may preserve direct interaction with hydrothermal systems, we use a reduced effective area of 3.6×10^6 km^2. *Carr and Chuang* [1997] calculated a globally averaged drainage density of 0.0032 km^{-1}. The product of effective area and drainage density, multiplied by typical valley width and height (5 km and 150 m, respectively), results in 8.6×10^3 km^3 of removed material. Sediment-to-water ratios may range from 1:4 to 1:1000 [*Gulick*, 1998, and references therein], implying that the volume of water required to erode the valleys was between 3.5×10^4 and 8.6×10^6 km^3, equivalent to a global water layer between 0.2 and 60 m deep. These values are well below the estimate of hundreds of meters for the global crustal inventory, indicating that discharge from the valleys had a negligible impact on the global water budget. They further imply that discharged water need not have been recharged to the crust.

[47] The total hydrothermal discharge produced is computed as follows. First, we assume that each magma chamber contributing to crustal formation intrudes into steady ambient temperature and pressure conditions; this is most likely if intrusions that formed the southern highlands moved between different loci rather than spreading from a single location [*Grimm*, 2000]. In this way, the discharge contribution from a single intrusion is just that of its equivalent HYDROTHERM model. We assume further that the crust covering the area occupied by valley networks (as calculated above) is eventually built up to a depth of 20 km by magma chambers packed side by side and one on top of the other. We sum the total discharges from each intrusion to calculate the total mass of surface water produced. We consider only those intrusions that contribute to magnetic anomalies, discarding other intrusive events. Determining the relative contribution of individual intrusions is not possible, but the probability p_0 may be used as an indicator of the appropriate fraction to be considered. Its value for a magnetic threshold of 10 nT, i.e., 0.469 (Table 2), is applied to all of our results.

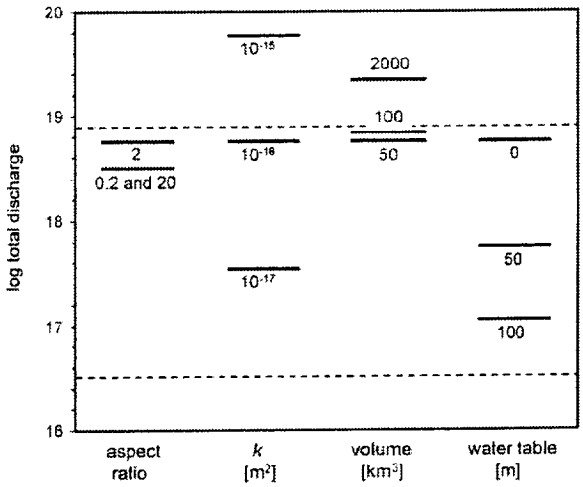

Figure 11. Summary of global discharge production (by mass, in kg) for various model parameters. The two dashed lines indicate the bounds on the mass of water required to erode the valley networks. Represented are discharge values for different magma chamber aspect ratios, for host rock permeabilities, for magma chamber volumes, and for the baseline model with different assumed water table depths. Note that the baseline model ($D/H = 2$, $k = 10^{-16}$ m^2, chamber volume = 50 km^3, water table depth = 0 m) appears in each vertical group of bars.

[48] A summary of discharge production over the entire region of interest is shown for different models in Figure 11. The two thick dashed lines denote the bounds on total required discharge. Represented are discharge values for different magma chamber aspect ratios (all with a volume of 50 km^3, host rock permeability of 10^{-16} m^2), host rock permeabilities (all chambers have $D/H = 2$ and a volume of 50 km^3), magma chamber volumes (all chambers have $D/H = 2$; host rock permeability is 10^{-16} m^2), and values for the baseline model with different assumed water table depths.

[49] All models meet or exceed the discharge production requirements, although it should be noted that if the $k = 10^{-17}$ m^2 model is assumed to have a water table of 100 m, its production will fall below the minimum required value. Other factors such as evaporation may further reduce the discharge available to carve valleys. The present evaporation mass flux is likely in the region of 4×10^{-8} kg m^{-2} s^{-1} [*Ingersoll*, 1974], which would reduce the effective discharge by as much as an order of magnitude or more. Ice may also reduce discharge (section 3.6). A 1 km thick layer of subsurface ice in our baseline model causes a 75% drop in total discharge. In models with other parameter values (e.g., greater magma chamber depth and smaller host rock permeability), ice may inhibit discharge more severely, if not completely.

5. Conclusions

[50] In numerical models of Martian hydrothermal systems we explored the control on surface discharge of magma chamber depth, volume, aspect ratio, and host rock permeability and porosity. Discharge has an approximately linear relationship to magma chamber volume and host rock permeability (in the range 10^{-17}–10^{-15} m^2). The influences of depth and aspect ratio are weaker, and that of porosity is negligible.

[51] Some geochemical aspects of Martian hydrothermal systems were considered by calculating water/rock ratios in our numerical models at various reaction temperatures. Ratios tend to be low but sufficiently large at mean permeabilities $>10^{-16}$ m^2 for

groundwater flow to be sustained, consistent with the expected storage of water in alteration assemblages. The presence of a short-lived vapor-dominated zone in our model with high host rock permeability (10^{-15} m^2) and shallow chamber depth (2 km) suggests that hydrothermal alteration processes may be responsible for the observed relative abundances of certain salts in the Martian soil, although other forms of alteration should not be excluded.

[52] Crustal formation processes which formed the magnetic anomalies observed on Mars today may have been attended by hydrothermal circulation that also provided surface water for valley network erosion. This idea is in agreement with the observed spatial correlation between magnetic anomalies and valleys and was tested further within the framework of a central hypothesis made up of two propositions. The first is that the magnetic anomalies formed as intruded crust and that the acquisition of thermoremnance occurred at relatively great depth. The second is that hydrothermal discharge attending global crustal formation processes is sufficient to provide the water necessary to carve the planet's valley networks.

[53] We tested this hypothesis using the numerical models described above, assuming that the crust was formed by the heterogeneously spaced and timed intrusion of multiple magma chambers, each of which produced the discharge predicted by its individual numerical model. We determined that many model configurations in the explored portion of the parameter space were capable of producing sufficient water to erode those valley networks statistically related to hydrothermal circulation. In particular, modest crustal permeabilities of 10^{-16}–10^{-15} m^2 can produce the discharge required to carve valleys and satisfy geochemical constraints, even in the presence of mitigating factors such as evaporation and finite water table depth.

[54] **Acknowledgments.** This work was supported by NASA grants NAG5-7190 and NAG5-9799. We thank Steve Ingebritsen and Dan Hayba for thoughtful reviews.

References

Acuña, M. H., et al., Global distribution of crustal magnetization discovered by the Mars Global Surveyor MAG/ER experiment, *Science*, *284*, 790–793, 1999.

Baker, V. R., Water and the Martian landscape, *Nature*, *412*, 228–236, 2001.

Baker, V. R., M. H. Carr, V. C. Gulick, C. R. Williams, and M. S. Marley, Channels and valley networks, in *Mars*, pp. 493–522, Univ. of Ariz. Press, Tucson, 1992.

Bonacina, C., G. Comini, A. Fasano, and M. Primicero, Numerical solution of phase-change problems, *Int. J. Heat Mass Transfer*, *16*, 1825–1832, 1973.

Burnett, M. S., D. W. Caress, and J. A. Orcutt, Tomographic imaging of the magma chamber at 12°50′N on the East Pacific Rise, *Nature*, *339*, 206–208, 1989.

Carr, M. H., *Water on Mars*, Oxford Univ. Press, New York, 1996.

Carr, M. H., and F. C. Chuang, Martian drainage densities, *J. Geophys. Res.*, *102*, 9145–9152, 1997.

Cathles, L. M., A. H. J. Erendi, and T. Barrie, How long can a hydrothermal system be sustained by a single intrusive event?, *Econ. Geol.*, *92*, 766–771, 1997.

Connerney, J. E. P., M. H. Acuña, P. J. Wasilewski, N. F. Ness, H. Rème, C. Mazelle, D. Vignes, R. P. Lin, D. L. Mitchell, and P. A. Cloutier, Magnetic lineations in the ancient crust of Mars, *Science*, *284*, 794–797, 1999.

Delaney, P. T., Rapid intrusion of magma into wet rock: Groundwater flow due to pore pressure increases, *J. Geophys. Res.*, *87*, 7739–7756, 1982.

Farmer, J., Hydrothermal systems on Mars: An assessment of present evidence, in *Evolution of Hydrothermal Ecosystems on Earth (and Mars?)*, pp. 273–299, John Wiley, New York, 1996.

Griffith, L. L., and E. L. Shock, Hydrothermal hydration of Martian crust: Illustration via geochemical model calculations, *J. Geophys. Res.*, *102*, 9135–9143, 1997.

Grimm, R. E., Magnetic lineations on Mars: Formation by Noachian crustal accretion or depletion?, *Proc. Lunar Planet. Sci. Conf. 31st*, abstract 2056, 2000.

Gulick, V. C., Magmatic intrusions and a hydrothermal origin for fluvial valleys on Mars, *J. Geophys. Res.*, *103*, 19,365–19,387, 1998.

Hayba, D. O., and S. E. Ingebritsen, The computer model HYDROTHERM, a three-dimensional finite-difference model to simulate groundwater flow and heat transport in the temperature range of 0 to 1,200°C, *U.S. Geol. Surv. Water Resour. Invest. Rep.*, *94-4045*, 1994.

Hayba, D. O., and S. E. Ingebritsen, Multiphase groundwater flow near cooling plutons, *J. Geophys. Res.*, *102*, 12,235–12,252, 1997.

Head, J. W., and L. Wilson, Mars: Formation and evolution of magma reservoirs (abstract), *Proc. Lunar Planet. Sci. Conf. 25th*, 527–528, 1994.

Hynek, B. M., and R. J. Phillips, Evidence for extensive denudation of the Martian highlands, *Geology*, *29*(5), 407–410, 2001.

Ingebritsen, S. E., and W. E. Sanford, *Groundwater in Geologic Processes*, Cambridge Univ. Press, New York, 1998.

Ingebritsen, S. E., and M. L. Sorey, Vapor-dominated zones within hydrothermal systems: Evolution and natural state, *J. Geophys. Res.*, *93*, 13,635–13,655, 1988.

Ingersoll, A. P., Mars: The case against permanent CO_2 frost caps, *J. Geophys. Res.*, *79*(24), 3403–3410, 1974.

Jakosky, B. M., and R. J. Phillips, Mars' volatile and climate history, *Nature*, *412*, 237–244, 2001.

Kieffer, H. H., Mars Consortium global maps, in *Third International Colloquium on Mars, LPI Contrib. 441*, pp. 133–135, Lunar and Planet. Inst., Houston, Tex., 1981.

Kletetschka, G., P. J. Wasilewski, and P. T. Taylor, Hematite vs. magnetite as the signature for planetary magnetic anomalies?, *Phys. Earth Planet. Inter.*, *119*, 259–267, 2000.

Kohlstedt, D. L., B. Evans, and S. J. Mackwell, Strength of the lithosphere: Constraints imposed by laboratory experiments, *J. Geophys. Res.*, *100*, 17,587–17,602, 1995.

Malin, M. C., and M. H. Carr, Groundwater formations of Martian valleys, *Nature*, *397*, 589–591, 1999.

Malin, M. C., and K. S. Edgett, Evidence for recent groundwater seepage and surface runoff on Mars, *Science*, *288*, 2330–2335, 2000.

Manning, C. E., and S. E. Ingebritsen, Permeability of the continental crust: Implications of geothermal data and metamorphic systems, *Rev. Geophys.*, *37*, 127–150, 1999.

McGill, G. E., Crustal history of north central Arabia Terra, Mars, *J. Geophys. Res.*, *105*, 6945–6959, 2000.

McSween, H. Y., and K. Keil, Mixing relationships in the Martian regolith and the composition of globally homogeneous dust, *Geochim. Cosmochim. Acta*, *64*, 2155–2166, 2000.

Newsom, H. E., J. J. Hagerty, and F. Goff, Mixed hydrothermal fluids and the origin of the Martian soil, *J. Geophys. Res.*, *104*, 8717–8728, 1999.

Norton, D., and J. Knight, Transport phenomena in hydrothermal systems: Cooling plutons, *Am. J. Sci.*, *277*, 937–981, 1977.

Pariso, J. E., and H. P. Johnson, Do layer 3 rocks make a significant contribution to marine magnetic anomalies? In situ magnetization of gabbros at Ocean Drilling Program Hole 735B, *J. Geophys. Res.*, *98*, 16,033–16,052, 1993.

Purucker, M., D. Ravat, H. Frey, C. Voorhies, T. Sabaka, and M. Acuña, An altitude-normalized magnetic map of Mars and its interpretation, *Geophys. Res. Lett.*, *27*, 2449–2452, 2000.

Raffensperger, J. P., and G. Garven, The formulation of unconformity-type uranium ore deposits, 2, Coupled hydrochemical modeling, *Am. J. Sci.*, *295*, 639–696, 1995.

Rye, R. O., P. M. Bethke, and M. D. Wasserman, The stable isotope geochemistry of acid sulfate alteration, *Econ. Geol.*, *87*, 225–262, 1992.

Schubert, G., S. C. Solomon, D. L. Turcotte, M. J. Drake, and N. H. Sleep, Origin and thermal evolution of Mars, in *Mars*, pp. 147–183, Univ. of Ariz. Press, Tucson, 1992.

Scott, D. H., and J. M. Dohm, Mars highland channels: An age reassessment, *Proc. Lunar Planet. Sci. Conf. 23rd*, 1251–1252, 1992.

Shock, E. L., Hydrothermal systems as environments for the emergence of life, *Ciba Found. Symp.*, *202*, 40–60, 1996.

Tanaka, K. L., J. M. Dohm, J. H. Lias, and T. M. Hare, Erosional valleys in the Thaumasia region of Mars: Hydrothermal and seismic origins, *J. Geophys. Res.*, *103*, 31,407–31,419, 1998.

Travis, B. J., N. D. Rosenberg, and J. N. Cuzzi, Geothermal heating, convective flow and ice thickness on Mars, *Proc. Lunar Planet. Sci. Conf. 32nd*, abstract 1390, 2001.

Turcotte, D. L., and G. Schubert, *Geodynamics*, John Wiley, New York, 1982.

Wasilewski, P. J., H. H. Thomas, and M. A. Mayhew, The Moho as a magnetic boundary, *Geophys. Res. Lett.*, *6*, 541–544, 1979.

R. E. Grimm, Blackhawk Geoservices, Inc., 301 B Commercial Road, Golden, CO 80401, USA. (grimm@blackhawkgeo.com)

K. P. Harrison, Laboratory for Atmospheric and Space Physics, University of Colorado, Campus Box 392, Boulder, CO 80309, USA. (keith.harrison@colorado.edu)